This is the accepted version of the following article: Wang WT, Li L*, Qu Z. Machine learning-based collapse prediction for postquake damaged RC columns under subsequent earthquakes. ***Soil Dynamics and Earthquake Engineering.*** This article may be used for non-commercial purposes.

Machine learning-based collapse prediction for postquake damaged RC columns under subsequent earthquakes

Wang Wentao[1], Li Lei[1,2*],Qu Zhe[3]

1. College of Civil Engineering, Xi'an University of Architecture and Technology, Xi'an, China

2. State Key Laboratory of Green Building in Western China, Xian University of Architecture & Technology, Xi'an, China

3. Institute of Engineering Mechanics, China Earthquake Administration, Harbin 150080, China.

Abstract:

The rapid assessment for numerous post-earthquake damaged reinforced concrete (RC) structures is critical for making informed post-earthquake decisions. However, this often requires significant resources in terms of manpower and calculation costs. This study proposes a machine learning (ML)-based method for predicting the collapse state of post-earthquake damaged RC columns under subsequent earthquakes, which are a critical earthquake-resistant component in RC structures. First, the damage strain field theory is introduced to establish the numerical analysis models for 10000 post-earthquake damaged RC columns. A dataset is constructed using time history analysis results obtained from these numerical analysis models under the action of 1,000 ground motion records. The Random Forest (RF) algorithm is then utilized to train an ML model that can predict the collapse state of post-earthquake damaged RC columns under subsequent earthquakes. To evaluate the accuracy of the ML prediction model, a testing dataset consisting of 47 full-size RC columns from the Pacific Earthquake Engineering Research Center (PEER) database is constructed. Results demonstrate that the prediction model has good accuracy, with an Area Under Curve (AUC) value and an F1 measure of 0.87 and 0.76, respectively. The SHapley Additive exPlanation (SHAP) algorithm is then utilized to interpret the ML prediction model, and the influences of design parameters, ground motion intensity parameters, and damage index on the prediction results are discussed. Finally, an interactive and user-friendly graphical user interface (GUI) tool is developed to provide a rapid collapse prediction of post-earthquake damaged RC columns. This study represents a pioneering step towards the application of ML in post-earthquake assessment for damaged RC columns.

Keywords

Post-earthquake; RC column; collapse; machine learning.

1 Introduction

The design of buildings based on the ductility concept typically results in superior collapse resistance. However, the collapse resistance of these buildings can be significantly reduced due to earthquake damage, leading to disastrous consequences [1]. In fact, subsequent earthquakes can sometimes cause more significant damage to structures than the initial earthquake, particularly for buildings that have been weakened by the initial earthquake. In this paper, subsequent earthquakes may represent aftershocks of the initial earthquake, or they may represent separate earthquakes (such as the double main shocks in the 2023 Turkey earthquake). Many practical cases have demonstrated the importance of evaluating the residual collapse resistance of post-earthquake damaged structures. For instance, in the 1976 Tangshan earthquake, many buildings and bridges that had survived the initial earthquake collapsed during the subsequent earthquakes. Similarly, during the Canterbury earthquake in New Zealand, the PGC building remained intact during the 7.1-magnitude initial earthquake in September 2010, but it collapsed during a 6.2 magnitude

* Corresponding author: Li Lei (lilei@xauat.edu.cn)

earthquake in February 2011. Consequently, it is essential to evaluate the residual collapse resistance of post-earthquake damaged RC structures. Over the past decade, the importance of assessing building-level post-earthquake collapse resistance has been highlighted, particularly in the context of quantifying seismic resilience at the individual infrastructure and community scales [2-3]. The reduced collapse resistance of buildings weakened by the initial earthquake has become a crucial indicator for evaluating the structural safety and acceptance criteria of post-earthquake damaged buildings. As a result, various countries have introduced different post-earthquake assessment guidelines [4-6]. These guidelines provide methods for post-earthquake visual inspection to rapidly evaluate building structural collapse safety. However, relying solely on the experience of assessment experts can reduce the efficiency of post-earthquake assessment work.

In recent years, machine learning (ML) methods have gained increasing importance in the risk and vulnerability assessment of building structures affected by natural disasters. ML is applicable to many types of risk assessment, from predicting structural component failure [7-8] to assessing regional building risk [9-10]. Compared to traditional techniques [4-6], ML methods have received more attention due to their high efficiency and accuracy. For example, Mangalathu [11] used ML methods to predict the failure mode of RC components. Harirchian [12] achieved a rapid classification of damage states in post-earthquake damaged RC structures using ML methods. Zhang [13] proposed an ML framework for assessing the post-earthquake safety of building structures. Miao et al. [14] developed and trained a deep convolutional network to estimate the strength and stiffness degradation of post-earthquake damaged RC columns. Xiong et al. [15] developed a post-earthquake damage assessment method for regional buildings based on unmanned aerial vehicles and deep learning. Jang [16] developed an assessment method for evaluating the serviceability of earthquake-damaged bridges using a deep learning network and visually inspected data. Luo et al. [17-19] and Paal et al. [20] proposed an artificial intelligence-enhanced algorithm capable of predicting the seismic response and damage state of RC frames. The results show that the suggested approaches perform better than conventional physics-based methods in terms of prediction accuracy and computational effectiveness. Existing research results indicated ML's capacity to effectively train a prediction model to predict the post-earthquake response of RC structures by learning from an informative dataset. However, most existing studies focus on predicting the initial earthquake responses and post-earthquake damage states of initial building structures, and similar studies on post-earthquake damaged structures are rare.

The methods used in the above studies share similarities in that they involve conducting dynamic time history analyses on numerical models of initial RC structures, and then constructing training datasets based on the dynamic response results to train the ML prediction model. The main difference among these studies lies in the utilization of various ML algorithms. However, when applying ML to predict the residual mechanical properties of post-earthquake damaged RC structures, it is typically necessary to construct numerical models and simulate their dynamic responses under the influence of subsequent earthquakes. This can be a challenging step due to the lack of available numerical analysis models for post-earthquake damaged RC structures, leading scholars to seek alternative methods. Currently, nonlinear dynamic analysis that considers mainshock-aftershock sequences is the primary method used to evaluate the residual seismic capacity of damaged components and structures. Salami et al. [21] performed a nonlinear dynamic analysis to investigate the vulnerability of rectangular and circular RC columns under bidirectional multiple excitations. Meanwhile, Abdelnaby et al. [22] established a numerical model that incorporates damage accumulation and investigated the degrading behavior of RC frames subjected to Tohoku and Christchurch earthquake sequences. Lu et al. [23] conducted an experimental study on the pseudo-static collapse of reinforced concrete (RC) frames and investigated the correlation between the collapse safety reserve coefficient and the displacement safety reserve

coefficient through nonlinear dynamic analysis. Maffei et al. [24] proposed four post-earthquake occupiability criteria based on different metrics used to assess the reduction in collapse safety of damaged buildings. Yeo and Cornell [25] used time-varying aftershock hazard at a site to determine an equivalent constant collapse rate, which decreases with time after the mainshock. Raghunandan et al. [26] quantified the increased vulnerability to collapse of modern ductile RC special moment frame buildings damaged by the mainshock. Burton and Deierlein [27] proposed a framework to evaluate the post-earthquake safety of damaged buildings. Shokrabadi and Burton [28] evaluated the residual capacities of damaged buildings in aftershocks. Abdelnaby [29] evaluated the failure probability of damaged RC frames in aftershocks. Iervolino et al. [30] studied the accumulation of seismic damage in RC structures subjected to multiple mainshock-aftershock sequences. However, the structural damage caused by mainshocks obtained through such methods may be inconsistent with the damage caused by real earthquakes [31], leading to inaccurate evaluation of the structure's resistance to aftershocks. Therefore, it remains challenging to accurately simulate the aftershock dynamic response of post-earthquake damaged RC structures, which limits the development of ML models for predicting the aftershock safety of these structures.

This study proposes a method for evaluating the collapse safety of post-earthquake damaged RC columns under subsequent earthquakes. The proposed method employs an ML model based on the random forest (RF) algorithm, which can predict the collapse state (collapse or safe) of arbitrary post-earthquake damaged RC columns subjected to arbitrary ground motion records. To establish the ML model, numerical analysis models for post-earthquake damaged RC columns are developed using the newly introduced damage strain field theory. The subsequent earthquake responses of these models are simulated through time history analysis to construct an ML dataset. Compared with nonlinear dynamic analysis considering mainshock-aftershock sequences, the proposed method can more accurately simulate the damage distribution and response of the post-earthquake damaged columns under subsequent earthquakes. The paper is organized as follows: section 2 details the methodology of the proposed method, section 3 presents numerical modeling and time history analysis of post-earthquake damaged RC columns, and section 4 establishes an ML prediction model for the collapse state of post-earthquake damaged RC columns based on RF and evaluates its accuracy and interpretability. At last, section 5 establishes an interactive, user-friendly graphical user interface (GUI) platform as an alternative to traditional mechanical techniques for the post-earthquake safety assessment of damaged RC columns.

2 Methodology

In this study, the RF algorithm was employed to evaluate the aftershock collapse safety of post-earthquake damaged RC columns, due to its demonstrated accuracy in previous studies. The RF algorithm is a type of integrated learning method that combines multiple decision trees to produce a final prediction based on voting. The ML algorithm is widely used for classification and regression tasks, and has better generalization ability compared to traditional decision trees and better interpretability compared to neural networks and support vector machines. The accuracy of the RF model is dependent on the quality of the dataset, which is comprised of a training set (used to build the prediction model) and a testing set (used to evaluate the performance of the model). Each sample in the dataset consists of two properties: sample features and sample classes. In this study, the sample features are design parameters of RC columns, damage index, and ground motion intensity parameters, while the sample classes represent the collapse states of post-earthquake damaged RC columns (safe or collapse). Prior to training the prediction model, the root node of any decision tree in the RF is populated with a subset of samples randomly selected from the total training dataset. At the start of training, the root node randomly selected a feature from among all the candidate features as the split feature.

The optimal splitting point was then determined by minimizing the weighted Gini index following node splitting, and the dataset in the root node was divided into two datasets, forming two new child nodes. The Gini index, also known as Gini impurity, is a metric representing the probability of misclassification for a randomly sampled item in the sample set. Its calculation method is expressed in Eq. (1).

$$Gini(p) = \sum_{k=1}^{K} p_k (1 - p_k) = 1 - \sum_{k=1}^{K} {p_k}^2 \tag{1}$$

where K is the total number of classes to which the sample may belong; p_k is the probability that the selected sample belongs to class k, and the probability that this sample is incorrectly classified is (1- p_k). The weighted Gini index is the weighted average of the Gini indexes of multiple datasets. The smaller the weighted Gini index is, the smaller the probability that the selected sample in the dataset is misclassified, that is, the higher the purity of the dataset; otherwise, the more impure the dataset is.

This paper briefly summarizes the classification principle of decision trees using Fig. 1 as an example. The root node in Fig. 1 selects feature A as the splitting feature, and then the optimal splitting point is determined using the gradient descent method. The dataset is then split with A=0.6 as the boundary to minimize the weighted Gini index of the resulting child nodes. During subsequent training, the child nodes randomly select features B and C for further splitting until the depth of the decision tree reaches the maximum value or the Gini index of the child node is 0. The decision tree is complete after multiple splits have been performed, resulting in a structure with one root node, multiple child nodes, and multiple leaf nodes. The leaf nodes are the lowest level of the decision tree, representing the end point of the classification process. The output of the leaf node is the class with the highest proportion among all sample classes in the leaf node. The RF algorithm includes multiple decision trees, each constructed with different features and root node samples. During prediction, a specific sample's features are input into each decision tree, which then classifies the sample based on the previously trained classification path. The final class of the sample is determined by a vote from all the decision trees.

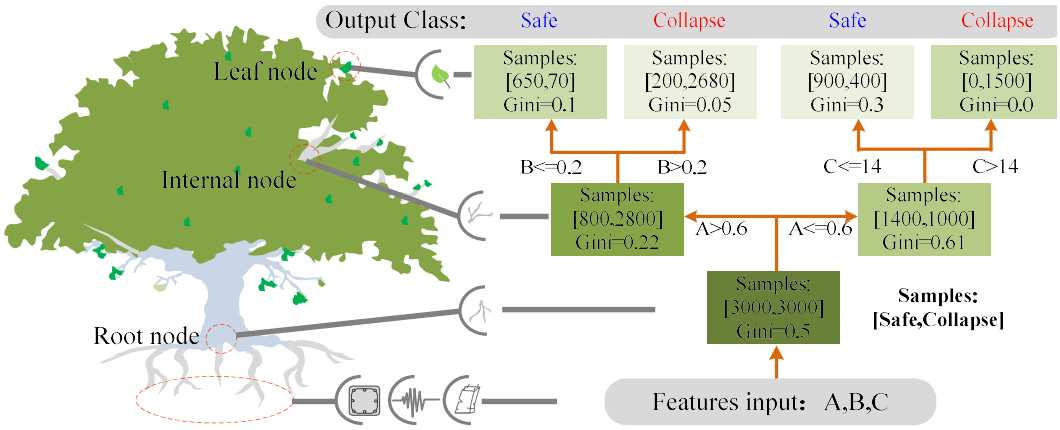

Figure 1. Decision tree classification algorithm ([x, y] means that the number of samples that belongs to the safe class in the node is x, and the number of samples that belongs to the collapse class in the node is y)

The RF algorithm is a supervised classification method that relies on manual annotation of both the sample features and classes in the training dataset to obtain accurate results. Consequently, a reliable training dataset is a necessary precondition for accurate training outcomes. However, numerical analysis models and test data for post-earthquake damaged RC columns are insufficient, which makes constructing a training dataset challenging. To address

this issue, this study established numerical models of post-earthquake damaged RC columns utilizing the damage strain field theory, and constructed a dataset from the time history analysis results to train the ML model for predicting the collapse states of post-earthquake damaged RC columns under subsequent earthquakes. The research method can be divided into several steps, as illustrated in Fig. 2. In the first step, 10000 numerical models of damaged RC columns with diverse design parameters and damage indices were randomly generated by utilizing the damage strain field theory. It is important to note that the damage strain field theory applies only to rectangular columns with bending failure, while cylinder and short columns with shearing failure were excluded. In the second step, 1000 ground motion records with different intensity parameters were selected from the PEER database for time history analysis of the numerical models, and six representative intensity parameters were chosen as sample features for the training set. In the third step, the established numerical models were randomly paired with the selected ground motion records, and then subjected to time history analysis. The collapse or safe states of the numerical models are determined by the results of the time history analysis. A collapse state is assigned when the maximum displacement ratio of the numerical model exceeds a specified limit during the time history analysis, whereas a safe state is assigned otherwise. In the fourth step, the design parameters and damage indices of the numerical models, along with the intensity parameters of the ground motion records, are treated as features, and the collapse or safe states of the numerical models is treated as the class for constructing a dataset. The RF algorithm is then employed to train a prediction model, which can predict the collapse state of a given post-earthquake damaged RC column (bending failure type) under the action of arbitrary ground motion record.

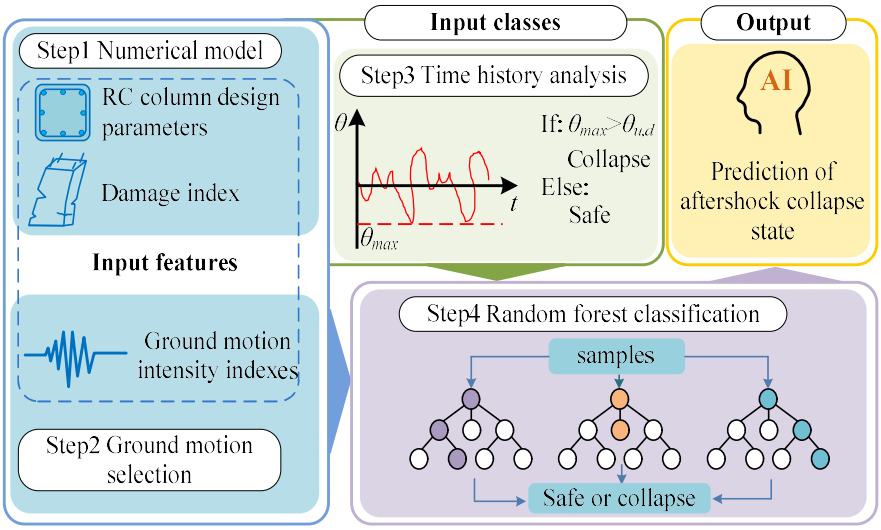

Figure 2. Overview of the machine learning-based collapse safety assessment method for post-earthquake damaged RC columns.(θ_{max} and $\theta_{u,d}$ are the maximum and ultimate drift rate response of columns, respectively)

3 Numerical modeling, time history analysis, and collapse state determination of post-earthquake damaged RC columns

3.1 Numerical modeling

3.1.1 Development of post-earthquake damaged RC columns

As previously mentioned, the construction of the training dataset for the ML prediction model in this study is based on numerical simulation. Thus, the development of a dependable numerical model that can effectively simulate

the residual load-displacement response of post-earthquake damaged RC columns is of utmost importance. In this section, numerical analysis models for post-earthquake damaged RC columns are established based on the authors' previous work[32], which introduced the damage strain field theory. The damage strain field theory aims to quantify the non-uniform distribution of seismic damage in RC columns. For RC columns with bending failure, Fig. 3(a) illustrates the damage distribution of internal materials in which the damage of materials is defined by the damage strain, i.e., the maximum strain experienced by local materials under seismic loads. The colors yellow, gray, and red respectively depict the damage strain distribution of cover concrete, confined concrete, and reinforcement. The darker the color, the larger the damage strain. After quantifying the damage distribution, the residual stress-strain relationships of damaged materials at various locations can be determined, as shown in Fig. 3(b). Subsequently, the residual load-displacement responses of post-earthquake damaged RC columns can be simulated using the fiber beam-column theory, as demonstrated in Fig. 3(c). The derivation of the damage strain field and the establishment process of the numerical model for post-earthquake damaged RC columns have been thoroughly detailed in the authors' previous work [32], and a brief introduction is presented in this secticon to ensure the completeness of the article.

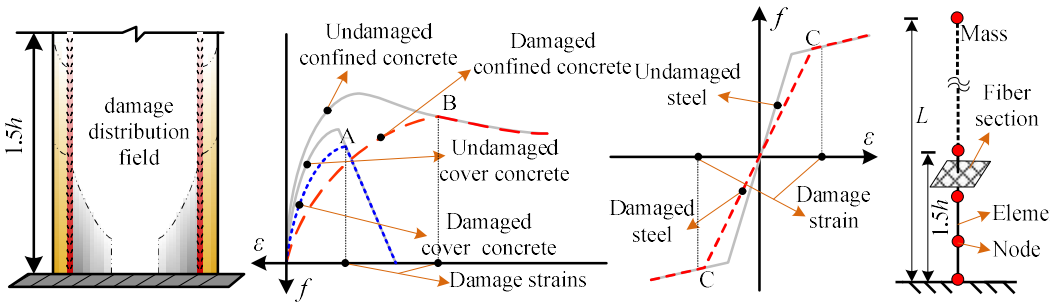

(a) Distribution of damage strain (b) Stress-strain relations of materials (c) numerical model

Figure 3. Damage strain distribution, material constitutive models, and finite element macroscopic model

According to Li [32], for RC columns with flexure failure type, the seismic damage is mainly concentrated within the height range of 1.5h(h is the section width) at the bottom of the columns (called damage zone). And the material damage strain within the damage zone is negatively exponentially distributed along the column height, and linearly along the depth of the section (plane section assumption). Li [32] summarized the distribution of material damage strain in RC columns with different damage degrees from existing test data. By regression, the damage strain field in the damage zone of post-earthquake damaged RC columns was quantified:

$$\varepsilon_d(e,\gamma)=\begin{cases}\dfrac{h_0-2(\gamma h-c)}{h_0}R(e)\cdot DI\cdot\varepsilon_{cc} & \text{if, } c/h<\gamma\le 0.5\\ \dfrac{h(1-2\gamma)}{h_0}R(e)\cdot DI\cdot\varepsilon_{cc} & \text{if, } 0\le\gamma\le c/h\end{cases} \tag{2}$$

where $\varepsilon_d(e,\gamma)$ is the damage strain of the sectional material at any location (e,γ) in the damage zone, $e=x/l_p$, $\gamma=y/h$, x is the height of the section from the bottom of the column, y is the length of the fibre from the loading surface of the column, h and h_0 are the height and net height of the column section, respectively. c is the thickness of the concrete cover, DI is the damage index, $R(e)$ is the sensitivity coefficient of damage related to e.

$$R(e)=\begin{cases}8.12\,exp(-e/0.3)+0.65 & if,\ 0.07\le e\le 1\\ 7.063 & if,\ 0\le e<0.07\end{cases} \tag{3}$$

The residual stress-strain relationship of the material at coordinate (e, γ) can be determined according to its damage strain $\varepsilon_d(e, \gamma)$, as shown in Fig. 3(b). If the damage strain $\varepsilon_d(e, \gamma)$ is greater than the peak strain of the material, the material is in the damage state, and its residual strength equals the stress corresponding to $\varepsilon_d(e, \gamma)$ on the stress-strain envelope, indicated as point A, B, and C in Fig. 3(b). If the damage strain $\varepsilon_d(e, \gamma)$ is lower than or equal to the peak strain of the material, the material can be considered undamaged, and the strength won't be degraded. The stress-strain relations of the cover concrete and confined concrete can be determined by Kent-Park model [33] and Mander model [34] (Eq. (4-5)).

$$\sigma_{c,d}(e,\gamma)=\begin{cases}f_{c,d}(e,\gamma)\left[\dfrac{2\varepsilon(e,\gamma)}{\varepsilon_c}-\left(\dfrac{\varepsilon(e,\gamma)}{\varepsilon_c}\right)^2\right] & \text{if},\varepsilon_d(e,\gamma)\le\varepsilon_c\\ f_{c,d}(e,\gamma)\left[\dfrac{2\varepsilon(e,\gamma)}{\varepsilon_d(e,\gamma)}-\left(\dfrac{\varepsilon(e,\gamma)}{\varepsilon_d(e,\gamma)}\right)^2\right] & \text{if},\varepsilon_c<\varepsilon_d(e,\gamma)\le\varepsilon_{cu}\end{cases} \tag{4}$$

where $\sigma_{c,d}(e, \gamma)$ and $\varepsilon(e, \gamma)$ denote the stress and strain of the damaged cover concrete at coordinates (e, γ), ε_c is the peak strain of the intact cover concrete, ε_{cu} is the ultimate strain of the intact cover concrete, $f_{c,d}(e, \gamma)$ is the residual strength of the damaged cover concrete which equals the stress corresponding to $\varepsilon_d(e, \gamma)$ on the stress-strain envelope, indicated as point A in Fig.3(b).

$$\sigma_{cc,d}(e,\gamma)=\begin{cases}\dfrac{f_{cc}\left(\varepsilon(e,\gamma)/\varepsilon_{cc}\right)r}{r-1+\left(\varepsilon(e,\gamma)/\varepsilon_{cc}\right)^r} & \text{if},\varepsilon_d(e,\gamma)\le\varepsilon_{cc}\\ \dfrac{f_{cc,d}(e,\gamma)\left(\varepsilon(e,\gamma)/\varepsilon_d(e,\gamma)\right)r}{r-1+\left(\varepsilon(e,\gamma)/\varepsilon_d(e,\gamma)\right)^r} & \text{if},\varepsilon_{cc}<\varepsilon_d(e,\gamma)\le\varepsilon_{ccu}\end{cases} \tag{5}$$

where $\sigma_{cc,d}(e, \gamma)$ and $\varepsilon(e, \gamma)$ denote the stress and strain of the damaged confined concrete at coordinates (e, γ), ε_{cu} is the peak strain of the intact confined concrete, ε_{ccu} is the ultimate strain of the intact confined concrete, $r=E_{cc}/(E_{cc}-E_{sec})$ is the shape coefficient; E_{cc} and E_{sec} are the elastic modulus and secant modulus of the intact confined concrete, respectively, $f_{cc,d}(e, \gamma)$ is the residual strength of the damaged confined concrete which equals the stress corresponding to $\varepsilon_d(e, \gamma)$ on the stress-strain envelope, indicated as point B in Fig.3(b).

The stress-strain relations for intact and damaged steel were simplified by a bi-linear model and can be defined by three parameters: yield strength, elastic modulus, and hardening modulus. The expressions for the equivalent yield strength of the damaged steel can be determined by Eq.(6). The equivalent elastic modulus of the damaged steel E_d equals $f_{y,d}(e, \gamma)$ divided by $\varepsilon_d(e, \gamma)$. The hardening modulus of the damaged steel is equal to that of intact steel.

$$f_{y,d}(e,\gamma)=\begin{cases}f_y & if,\varepsilon_d(e,\gamma)\le\varepsilon_y\\ f_y+E_{s,h}\left(\varepsilon_d(e,\gamma)-\varepsilon_y\right) & if,\varepsilon_y<\varepsilon_d(e,\gamma)\end{cases} \tag{6}$$

where f_y and ε_y denote the yield strength and the corresponding strain of the intact steel, $f_{y,d}(e, \gamma)$ denotes the equivalent yield strength of the damaged steel (indicated as point C in Fig.3(b)), $E_{s,h}$ is the hardening modulus of the intact steel.

The residual stress-strain relations of the damaged materials can be determined by substituting their damage strain into Eq. (4) to (6).

After determining the residual stress-strain relationships of damaged materials, the numerical modeling and analysis can be carried out based on the fiber beam-column element theory. The establishment of the numerical model in this study is based on the OpenSees platform. The macroscopic diagram of the finite element model is shown in Fig. 3(c). In Fig. 3(c), L is column height and h is section height, and displacement-based beam-column element(DBE) is used. DBE is based on the fiber section theory, once the fiber stress-strain relation at each position on the section is determined, the stiffness matrix of the section and element can be solved. In this study, the fiber section is divided into 50 fibers along the section height and width to ensure the calculation accuracy and efficiency [35-36]. The cover concrete and the confined concrete are simulated using concrete 02 and concrete 04 material in OpenSees respectively, and the steel fiber is simulated using Hysteretic material in OpenSees.

To ensure the generalizability of the ML prediction model, the numerical models constructed in this study should cover comprehensively the potential distribution range of the major design parameters of RC columns. In this study, all the design parameters (listed in Table 1) of the 10000 numerical models were randomly generated within the range specified by the code GB 50011-2010 [37]. By using this method, the generated numerical models can include various types of RC columns, while also possibly generating some unrealistic designed RC columns. These unrealistic designed RC columns may be relatively rare in practical engineering, but they still objectively exist, especially in some old buildings in China. When constructing the training set, if only the well-designed RC columns are considered, the ML model may not be able to assess the residual seismic capacity of those poor-designed buildings effectively. The parameter generation method proposed in this study can make the values of all parameters uniformly distributed throughout the entire feature space, thereby making the generated dataset more diverse and extensive[39-40]. The trained model can be used to predict a wider variety of RC columns, not just well-designed ones, and can also avoid the risk of overfitting in the dataset. Although this method may generate some RC columns with unreasonable design parameters, the existence of these RC columns will not have too much negative impact on the random forest algorithm. This is because the random forest is based on multiple decision trees, each of which is trained on different features and subsets of samples, giving it strong resistance to outliers. During training, the anomalous data is likely to be assigned to a particular tree without affecting the overall decision of the random forest. Furthermore, when making statistical decisions, the random forest typically employs the majority voting method, which combines the results of multiple decision trees to determine the final result, further increasing the algorithm's robustness to outlier data.

Subsequently, a computer program was developed to create 10,000 OpenSees finite element models of RC columns with distinct design parameters and damage degrees. The fundamental periods of the generated models were calculated and plotted, as depicted in Fig. 4. The normal distribution of the fundamental period distribution can be observed from Fig. 4.

Table 1 Distribution ranges of design parameters of numerical models

Parameter	f_c/MPa	f_y/MPa	f_{yv}/MPa	ρ_s	ρ_{sv}	B_s	DI	N_0	N_v	h/mm
Range	20~40	300~600	300~600	0.6%~5%	0.4%~5%	0~0.05	0~1	0~0.9	4~8	200~500

Where: f_c is the concrete compressive strength, f_y is the yield strength of the longitudinal reinforcement, f_{yv} is the yield strength of the stirrup, ρ_s is the section reinforcement rate, ρ_{sv} is the volumetric stirrup ratio, B_s is the hardening rate of the longitudinal reinforcement, N_0 is the axial compression ratio, N_v is the shear span ratio.

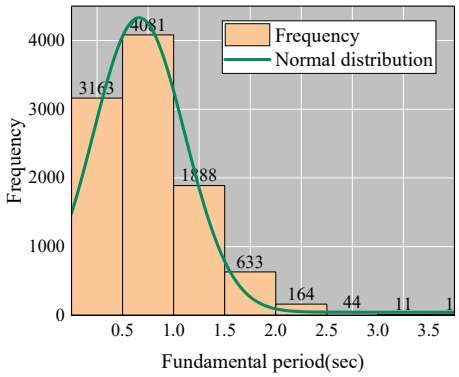

Figure 4. The fundamental period distribution of numerical models of post-earthquake damaged RC columns

3.1.2 Validation of the development of post-earthquake damaged RC columns

Although the numerical modeling technique for post-earthquake damaged RC columns presented in section 3.1.1 has been validated by author's previous work [32], the reasonability is further verified in this study using the test data of 47 rectangular full-size RC columns with flexure failure mode in PEER database [40-51]. Details of the selected test columns are shown in Appendix A1. At the same time, these test data will also be used to construct the testing dataset to verify the ML prediction model in section 4.2. First, based on the numerical simulation method proposed in Section 3.1.1, 235 numerical models were established for 47 test columns under intact, slight, moderate, severe, and extremely damaged conditions (*DI*= 0, 0.2, 0.4, 0.6, 0.8). To facilitate replication of the proposed methodology, Table A.2 displays the damage strain and ultimate strain of the extreme fibers of confined concrete in the bottom section of the 47 test columns. The numerical simulation method is verified by comparing the simulated residual load-displacement response of the test columns under different damage states with the test results. By substituting *DI* of the test RC columns under different damage states into the two-parameter damage model proposed by Park and Ang [52](Eq. 7), the corresponding peak deformation of RC columns under any *DI* can be calculated. After the peak deformation is obtained, the residual load-displacement response of RC columns under different damage states can be obtained by splitting the complete load-displacement curve of RC columns and comparing it with the simulation results.

$$DI = \frac{x}{x_u} + \beta \frac{\int dE}{F_y x_u} \tag{7}$$

where x is the actual maximum deformation of the column during the loading process. x_u is the monotonous ultimate deformation of the column, dE is the cumulative hysteretic energy dissipation, F_y is the yield force, and β is the energy dissipation coefficient.

An illustration of the residual load-displacement responses for Ang. No. 3 specimen is presented in Fig. 5(a)-(d) as an example, where the solid green line denotes the model results and the dashed origin line represents the test results. The simulation results of residual load-displacement responses under different damage states are found to be in good agreement with the test results. Fig. 5(e)-(h) compare the model results and the test results of the residual bearing capacity of all the columns in various damage states. The model results exhibit good agreement with the test results, with most columns having bearing capacity errors of less than 15%, while only a few columns' errors exceed 15%

under severe and extreme damage states. Overall, the accuracy of the simulation results is acceptable. Hence, the proposed numerical model in this study can effectively predict the residual load-displacement response of RC columns under different damage states, and it is reasonable to pursue further study based on the proposed numerical modeling technique.

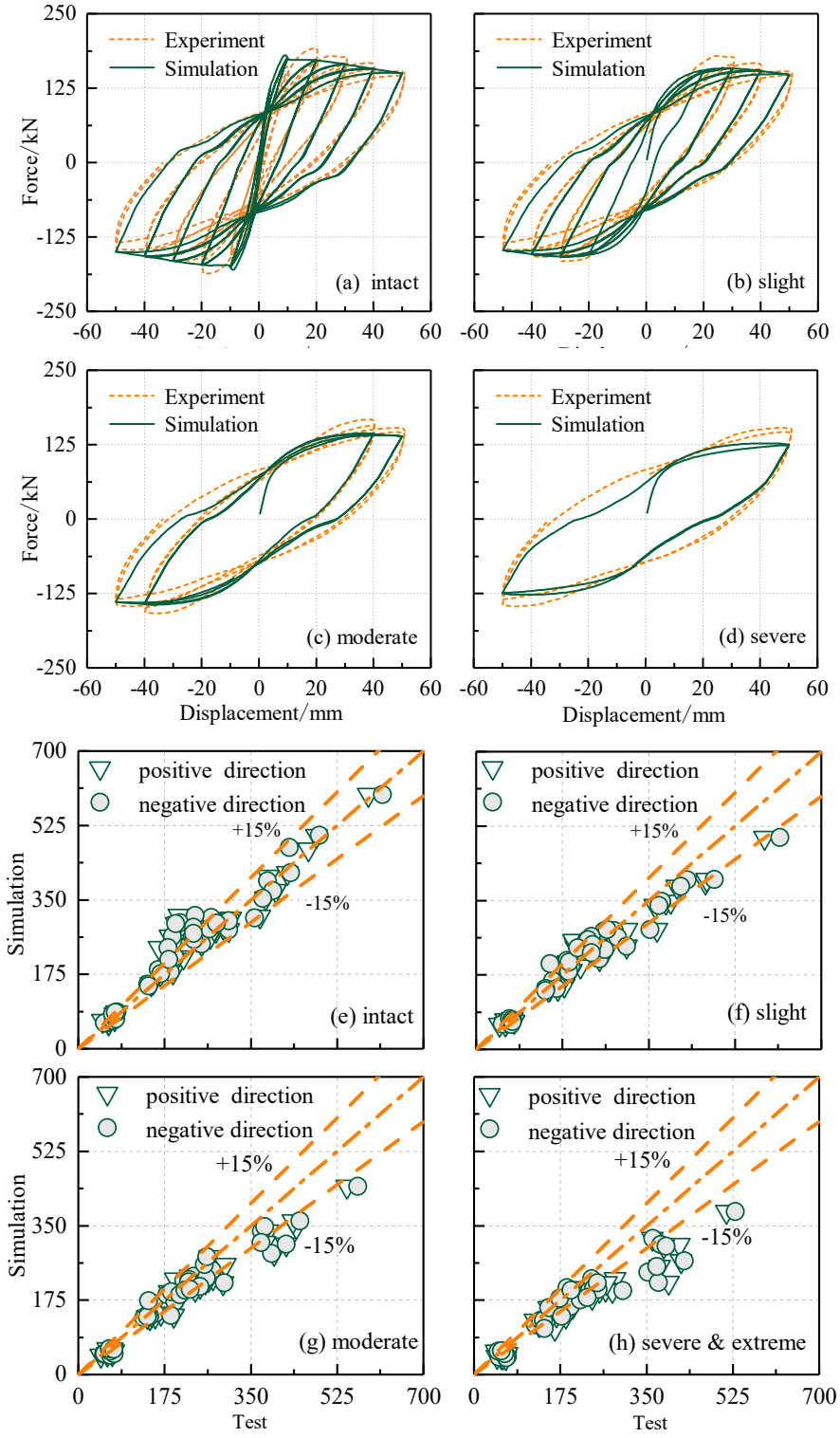

Figure 5. Comparison of residual load-displacement responses and bearing capacity of test columns under different damage states between test and simulated results

3.2 Time history analysis

3.2.1 Ground motion intensity parameters and ground motion records selection

The commonly used ground motion intensity parameters in structural seismic analysis can be divided into three types: acceleration-related, velocity-related, and displacement-related. Previous research indicates that different RC structures exhibit varying degrees of sensitivity to different types of ground motion intensity parameters. For example, RC columns with lower fundamental periods (T_1<0.5) are more sensitive to changes in acceleration-related intensity parameters, while RC columns with larger fundamental periods (T_1>0.5) are more sensitive to changes in velocity-related and displacement-related intensity parameters. Therefore, it is necessary to comprehensively consider the influence of different types of ground motion intensity parameters when predicting the collapse states of RC columns under subsequent earthquakes.

Within the same type of ground motion intensity parameters, several distinct parameters exist. For example, under the intensity parameter classification of acceleration-related, there are more than ten common parameters, such as peak acceleration, square root acceleration, and root mean square acceleration. However, some parameters' expressions are similar, leading to information overlap among parameters. Therefore, further screening of these intensity parameters is required. According to Wu [53], six representative parameters are selected as ground motion intensity indicators in this study, which also cover acceleration-related, velocity-related, and displacement-related types, as shown in Table 2.

Table 2 Definition and distribution of ground motion intensity parameters

Parameters	Definition	Dimension	Range	Mean value	Median	Skewness
Acceleration spectral intensity	$I_{sa}=\int_{0.1}^{0.5}S_a\left(T,\xi=5\%\right)dT$	g·sec	[0.04,0.79]	0.35	0.33	0.44
Arias intensity	$I_A=\frac{\pi\int_0^{t_f}\left[\ddot{u}_g(t)\right]^2dt}{2g}$	cm/sec	[0.03,19.4]	4.53	3.48	1.61
Peak velocity	$V_{pg}=max\left\|\ddot{u}_g(t)\right\|$	cm/sec	[2.41,64.82]	23.63	21.44	0.89
Velocity spectral intensity	$I_{sv}=\int_{0.1}^{0.25}S_v\left(T,\xi=5\%\right)dT$	cm	[7.82,299.45]	106.41	97.58	0.86
Cumulative absolute displacement	$D_c=\int_0^{t_f}\left\|\ddot{u}_g(t)\right\|dt$	cm	[21.57,1195.99]	346.40	306.45	1.22
Peak displacement spectrum	$S_{d,max}=max\left(S_d\left(T\right)\right)$	cm	[0.71,100.47]	25.27	21.92	1.06

To comprehensively cover the general distribution range of the selected intensity parameters, 1000 different real ground motion records were randomly selected from the PEER database in this study. The peak acceleration range of the selected ground motion records is 52-8302 cm/s^2, which covers the range of the peak acceleration of rare

earthquakes of magnitude 6-9 as stipulated in GB 50011-2010 [37]. Among them, there is 200 Class I sites, 530 Class II sites, 310 Class III sites, and 60 Class IV sites, which fully cover the four types of site soil stipulated in GB 50011-2010 [37]. The distribution of intensity parameters of the 1000 selected ground motion records is shown in Table 2 and Fig. 6. The skewness of each intensity parameter data is within the range of 0-1.7, which passes the normal distribution test. It can be observed that the 1000 ground motion records screened in this study not only satisfy the assumption of normal distribution of data but also encompass various possible earthquake types and intensities.

It should be noted that the focus of this study is on predicting the collapse probability of post-earthquake damaged RC columns under subsequent earthquakes. When screening subsequent earthquakes used to input the model, the selected earthquakes were not only real aftershock records but also included many mainshock records. Recent earthquakes in Turkey have shown that the intensity of subsequent earthquakes may be comparable to or even exceed that of the first one. These subsequent earthquakes in the Turkish earthquake are considered by most scholars to be independent earthquakes (double mainshocks) rather than aftershocks of the initial earthquake. In such cases (excited by high-intensity subsequent earthquakes), the ML model trained solely on aftershocks may exhibit poor predictive performance.

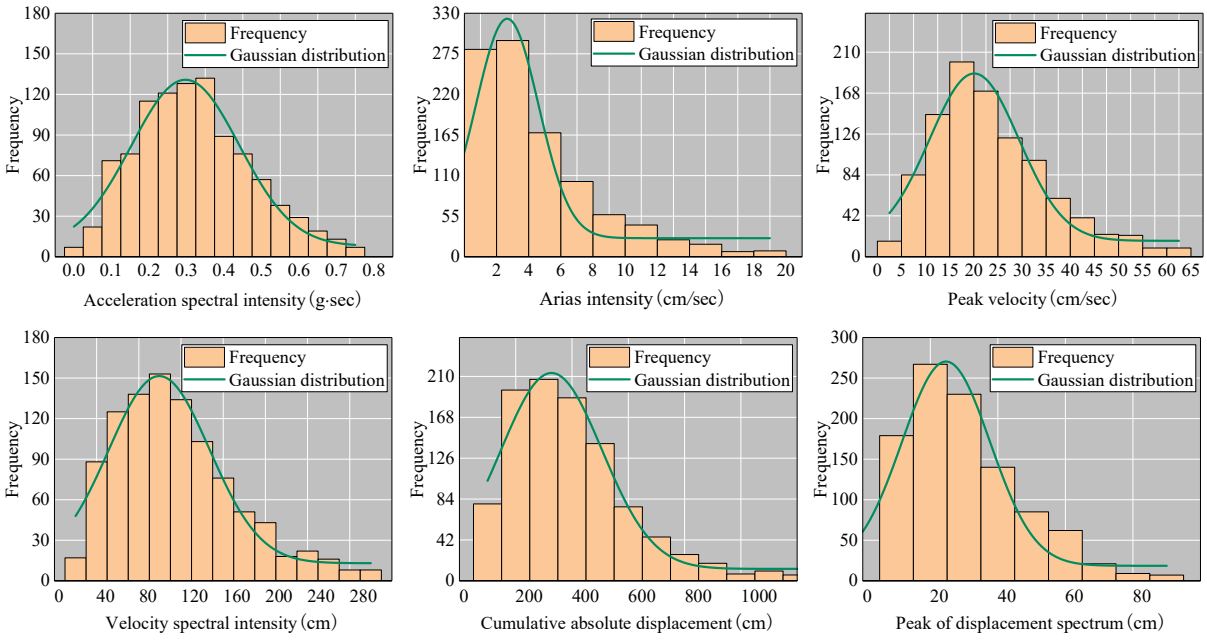

Figure 6. The intensity parameter data distribution of screened ground motion records

The Pearson correlation coefficient ρ_{xy} was used to quantify the degree of linear correlation between the parameters to verify that there was no high information overlap among the selected parameters. Pearson correlation coefficient between the two parameters x and y can be calculated as follows:

$$\rho_{xy} = cov(x, y) / \sigma_x \sigma_y \tag{8}$$

where $cov(x, y)$ is the covariance of variables x and y; σ_x and σ_y are the standard deviations of the variables x and y, respectively. The greater ρ_{xy} is, the higher the correlation between parameters is. When the absolute value of ρ_{xy} is less than 0.8, it can be considered that the degree of information overlap between parameters is low. The distribution cloud map of the Pearson correlation coefficient among various parameters of 1000 screened ground motion records is

shown in Fig. 8. It can be seen that the Pearson correlation coefficient among different parameters is less than 0.8, indicating that there is not too much information overlap among the selected parameters.

3.2.2 Time history analysis results

After randomly pairing the numerical models established in Section 3.1 with the selected ground motion records, time history analysis of the numerical models was conducted using OpenSees. The response of each model's maximum drift ratio is presented in Fig. 8. As illustrated in Fig. 8, the distribution of the maximum drift ratio for the numerical models conforms to a normal distribution, indicating that the numerical models effectively cover a variety of damage states for the post-earthquake damaged columns.

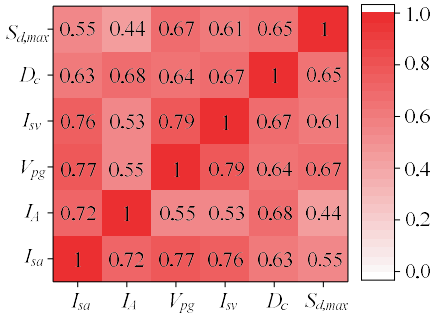

Figure 7. Correlation coefficient distribution of ground motion intensity parameters

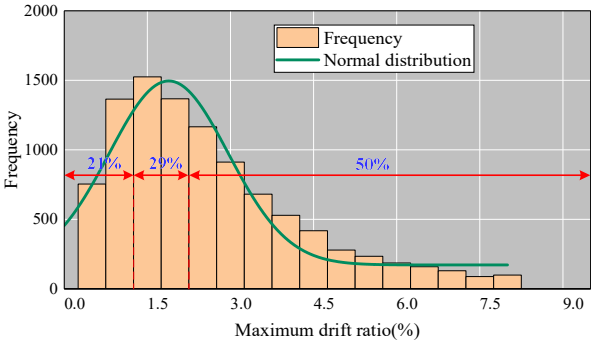

Figure 8. Distribution of time history analysis results (maximum drift ratio)

3.3 collapse state determination

In this study, the collapse states of RC columns under subsequent earthquakes are determined according to the response of the maximum drift ratio in time history analysis. The RC column is considered to be in collapse state when its maximum drift ratio response exceeds its ultimate drift ratio. In this study, the calculation method provided in ASCE 41-17 [54] was used to determine the ultimate drift ratio of RC columns:

When $N_0 \leq 0.5$:

$$\theta_u = 0.7 \cdot max\left(\frac{0.5}{5 + N_0 f_c / 0.8\rho_t f_{yv}} - 0.01, K \right) \tag{9}$$

where θ_u is the ultimate drift ratio of RC columns, ρ_t is the stirrup rate, and the parameter K can be calculated according to:

$$K = max\left(0.042 - 0.043N_0 + 0.63\rho_t - 0.023\frac{V_y}{V_{col}}, 0 \right) \tag{10}$$

where V_y is the shear force of RC columns at yield, V_{col} is the shear capacity of RC columns.

When $0.5 < N_0 \leq 0.7$:

$$\theta_u = \theta_{u,N_0=0.5} - (N_0 - 0.5)\frac{\theta_{u,N_0=0.5} - max(K,0)}{0.2} \tag{11}$$

When $N_0 > 0.7$, $\theta_u = max(K,0)$. Previous studies have demonstrated that the damage caused by the mainshock to columns reduces their drift capacity in subsequent earthquakes, leading to lower ultimate drift ratios in damaged

columns as compared to those prior to earthquakes [5]. In FEMA 306 [5], the ultimate drift ratio of damaged RC columns can be estimated by introducing the degradation coefficient λ_D:

$$\theta_{ud} = \theta_u \lambda_D \tag{12}$$

where θ_{ud} is the ultimate drift ratio of damaged RC columns, and λ_D is the degradation coefficient. According to FEMA306, the degradation coefficients λ_D can be estimated as 1.0, 0.9, 0.8, and 0.7 respectively for RC columns in minor (DI=0.2), moderate(DI =0.4), severe(DI =0.6), and extreme(DI =0.8) damage. The degradation coefficient in this study was determined by linear interpolation according to FEMA 306.

4 Development, validation, and interpretability of ML model

4.1 Dataset generation and basic parameters of ML model

4.1.1 Generation of the training dataset

Based on the collapse criterion specified in Section 3.3, the collapse states of the numerical models established in Section 3.1 were determined. Specifically, 5878 numerical models were found to be in the safe state while 4122 were in the collapsed state. Utilizing the numerical model design parameters outlined in Table 1, along with the damage index and ground motion intensity parameters presented in Table 2, a binary classification model was developed. Specifically, the post-earthquake collapse state of the models was considered as the binary response variable, and the aforementioned features were used as predictors. Through this approach, a training dataset consisting of 10,000 data points was generated.

4.1.2 Generation of the testing dataset

In this section, a testing dataset is constructed using the test data of 47 full-size RC columns from the PEER database to verify the accuracy of the ML prediction model. The testing dataset was generated based on 235 numerical models of the 47 test columns under different damage states, as established in Section 3.1.2. For each numerical model, 10 time history analyses were performed using ground motion records randomly selected from the 1000 ground motion records in Section 3.2. Following each time history analysis, the collapse state of the numerical model was determined. It should be noted that the ultimate drift ratio of the RC columns in the testing dataset was determined based on real test results, rather than the equations in Section 3.3. After completing these steps, a testing dataset comprising 2350 data points was formed. The number of samples in the safe state was 1436, and that in the collapsed state was 914.

4.1.3 basic parameters of the ML model

Prior to training the dataset using the random forest algorithm, it is essential to define several critical parameters in the algorithm program. Commonly used custom parameters in the random forest algorithm include the maximum feature number, maximum depth, and the number of decision trees. In general, a larger maximum feature number and depth tend to produce better training effects of the algorithm on the dataset. However, excessive feature numbers and decision tree depth may lead to overfitting, resulting in a poor prediction effect of the ML model on the testing dataset. With a larger number of decision trees, the random forest usually converges to a lower generalization error. When the number of decision trees exceeds a certain value, the model error essentially converges. Further increase in the number of decision trees at this stage fails to enhance the prediction effect. In this study, the network structure of the random forest algorithm is determined by grid search as 500 decision trees with a depth of 10 layers, with the maximum feature of each decision tree set to None.

4.2 Predictive performance of ML model

The assessment of binary ML prediction models often involves measuring the AUC value and F1 score. AUC (Area Under Curve) is calculated as the area under the Receiver Operating Characteristic (ROC) curve. Originally developed in signal detection theory, ROC curves are now commonly used in machine learning to evaluate the classification performance and generalization of ML models. To introduce ROC curves, it is necessary to first define the confusion matrix, which contains four key parameters: true positives (TP), false positives (FP), false negatives (FN), and true negatives (TN). TP represents the number of samples predicted as positive and actually belonging to the positive class, while FP represents the number of samples predicted as positive but actually belonging to the negative class. Similarly, FN represents the number of samples predicted as negative but actually belonging to the positive class, and TN represents the number of samples predicted as negative and actually belonging to the negative class. Using the confusion matrix, the true positive rate (TPR) and false positive rate (FPR) of the prediction results can be calculated:

$$\mathrm{FPR} = \frac{\mathrm{FP}}{\mathrm{FP} + \mathrm{TN}} \tag{13}$$

$$\mathrm{TPR} = \frac{\mathrm{TP}}{\mathrm{TP} + \mathrm{FN}} \tag{14}$$

where TPR refers to the ratio of the predicted number of safe samples to the actual number of safe samples, whereas FPR is the ratio of the number of samples predicted to be safe but actually classified as collapse to the actual number of collapse samples. A coordinate point on the ROC curve can be obtained by plotting FPR on the X-axis and TPR on the Y-axis. In the RF algorithm, the sample is classified as safe or collapse based on whether the probability exceeds a decision threshold. By varying the decision threshold, different confusion matrices and (FPR, TPR) coordinate points can be obtained. Connecting these coordinate points generates a complete ROC curve, and the AUC value represents the area enclosed under the ROC curve. A larger AUC value generally indicates a better prediction ability of the ML model. Furthermore, the higher the AUC value, the lower the misclassification rate, implying that the model is more inclined to avoid misclassifying samples actually classified as safe as collapse. The AUC value of the ML model is inversely proportional to its misclassification rate, indicating that the model is more likely to accurately predict safe samples and avoid misclassifying them as collapse. A higher AUC value facilitates the maximum utilization of buildings that can still be used after repair during the post-earthquake assessment, thereby reducing reconstruction costs. However, there is a risk that some buildings with a greater risk of collapse may be erroneously classified as safe, which increases the risk of injury or death to the building occupants. The F1 measure is another metric used to evaluate the performance of prediction models, focusing on precision and recall. A higher F1 measure indicates lower missing prediction rates, meaning that more collapsed samples can be predicted. During post-earthquake rescue and assessment operations, buildings that have not collapsed in the initial earthquake may need to be temporarily occupied. A higher F1 measure helps ML predictive models accurately identify buildings at high risk of collapse in potential under subsequent earthquakes, thereby avoiding temporary occupancy of these buildings and reducing the risk of injury and death for building occupants. In this study, both the AUC value and F1 measure were utilized to evaluate the ML prediction model, aiming to develop a model with high economic benefits while minimizing the risk of injury or death to building occupants. The F1 measure can be calculated using Eq. (15):

$$\mathrm{F1} = 2\left(\mathrm{PRE} \cdot \mathrm{REC}\right) / \left(\mathrm{PRE} + \mathrm{REC}\right) \tag{15}$$

where PRE is the precision, PRE=TP/(TP+FP); REC is the recall, REC= TP/(TP+FN).

The theoretical values of AUC and F1 are between 0 and 1, and the closer the value is to 1, the stronger the classification ability of the prediction model is. The ROC curve and confusion matrix of the prediction model on the testing dataset are shown in Fig. 9-10. The values of AUC and F1 calculated according to Fig. 9-10 are 0.87 and 0.76 respectively, indicating that the ML prediction model has a good classification ability. As can be seen from Fig. 10, 425 samples were wrongly predicted, accounting for 18% of the total number of samples, that is, the accuracy of the ML prediction model reached 82%.

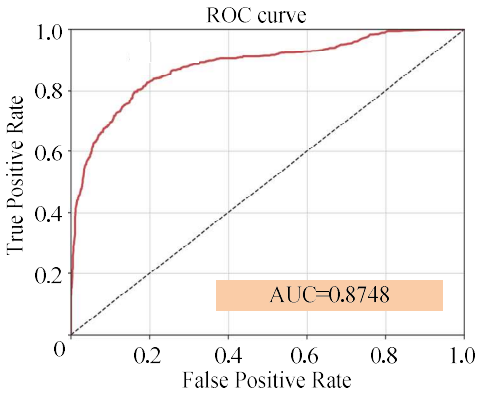

Figure 9. ROC curve

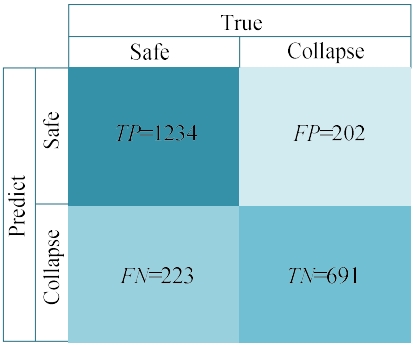

Figure 10. confusion matrix

4.3 Interpretability of ML model

Although ML models are effective in solving classification and regression problems, their interpretability has been difficult to elucidate. The SHapley Additive exPlanation (SHAP) method, derived from game theory, has emerged as a promising technique for addressing the interpretability of ML models. This method evaluates the importance of an individual by calculating their contribution to the cooperation, thus reflecting how each sample feature influences the prediction outcome. SHapley value refers to the contribution of each feature in each sample, while Additive Shapley values refer to the cumulative contribution of each feature across all samples. Furthermore, exPlanation refers to the explanation of a single sample, i.e., how each feature affects the predicted outcome of the ML model. In this study, the Tree SHAP algorithm, which is suited for tree models, is used to explain the ML prediction model.

Fig. 11 displays the global importance coefficient of each input feature. The mean SHAP value, which is estimated as the average of the absolute Shapley value of each feature in the dataset, is used to rank the input features in order of importance. The importance of each feature can be determined by the magnitude of its mean SHAP value. It is important to note that the importance coefficients in the figure are relative values, and are solely intended for comparing the relative importance between input features. Features with low importance coefficients are not necessarily insignificant. The analysis of Fig. 11 indicates that the axial compression ratio N_0, velocity spectral intensity $I_{sv,}$ and volumetric stirrup ratio ρ_{sv} are the three most important features. On the other hand, hardening rate B_s, Arias intensity $I_{A,}$ and cumulative absolute displacement D_c are the three least important features. The damage index DI is ranked as the fourth most important feature, following ρ_{sv}.

It can be seen from Figure 11 that the intensity parameters of subsequent earthquakes have a great contribution to the collapse of damaged RC columns. It is important to note that, the focus of this study is on predicting the collapse probability of post-earthquake damaged RC columns under subsequent earthquake excitation. The dataset of the

earthquakes which includes mainshocks can help to obtain machine learning models with high compatibility. Therefore, the earthquakes screened in this study include both mainshock and aftershock records to cover more types of earthquakes. In fact, the type of subsequent earthquake that damaged structures encounter is more likely to be a smaller aftershock than an independent larger earthquake. Therefore, in Figure 11, the intensity parameters of subsequent earthquakes are of greater importance. Based on this consideration, the importance of aftershocks to the collapse of damaged RC columns is further discussed by excluding the mainshock records in the dataset.

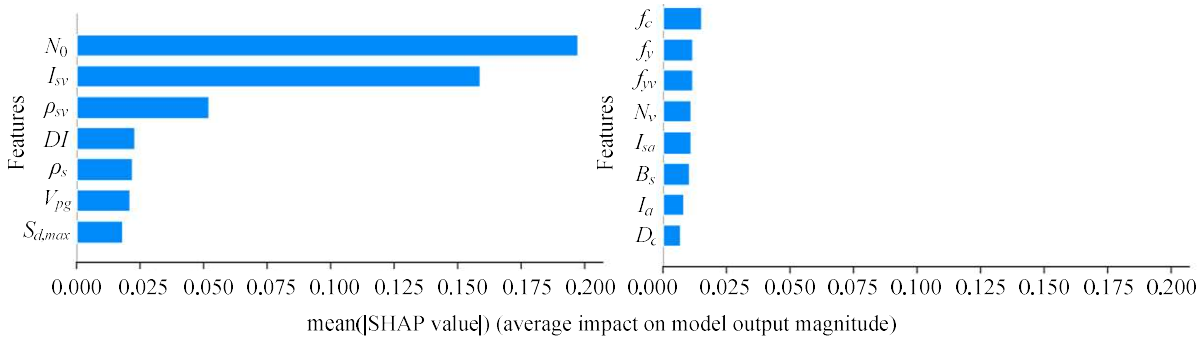

Figure 11. Importance factor of each input feature for the column database.

By excluding the mainshocks in the training set, the contribution of aftershocks to the collapse of damaged RC columns can be quantified at the global level. According to Salami's research [21], aftershocks make different contributions to the collapse probability of RC columns with different damage degrees. Therefore, this study classified damaged RC columns according to the damage index (slight damage, moderate damage, severe damage, and extreme damage), and discussed respectively the contribution of aftershocks to the collapse of damaged RC columns under different damage degrees, as shown in Fig. 12.

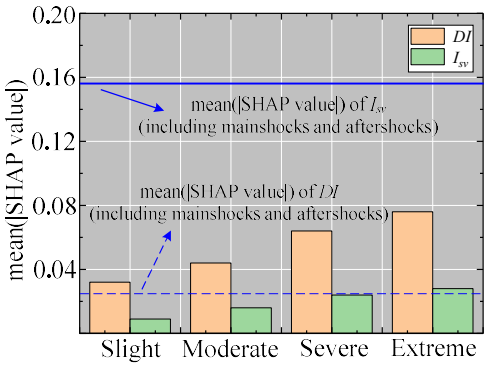

Figure 12. The importance factor of features *DI* and I_{sv} in different damage degrees(only aftershocks)

The analysis presented in Figure 12 reveals that excluding the mainshocks in the training set results in an increased contribution of the damage index to collapse, accompanied by a substantial decrease in the contribution of aftershock intensity to collapse. Moreover, as the damage degree escalates, the contribution of the damage index (mainshock damage) to collapse increases. Despite being consistently smaller than the damage index, the contribution of aftershocks to collapse remains significant. Taking extreme damage as an example, the feature importance factor of the mainshocks(*DI*) is 0.076, and the total feature importance of the mainshocks and aftershock is 0.104 (sum of

the feature importance factors of *DI* and I_{sv}), representing a 36.8% increase. This indicates the significant impact of aftershocks, which is consistent with the findings of previous research[22].

Interpreting model predictions at the individual sample level is important for gaining a deeper understanding of how input features influence the final prediction result. Compared to global importance, the local importance of features is not affected by the inclusion of more mainshocks in the earthquake dataset. This study illustrates this concept by presenting two samples from the testing dataset, specimens Lynn. 2CLH18 [48] and Saatcioglu. BG-1 [49], to demonstrate how SHAP decomposes the predicted results into the sum of influences of each input feature (Fig. 13 and Fig. 14). The ML prediction model accurately predicted the state of specimen Lynn.2CLH18 as safe, but incorrectly predicted the state of specimen Saatcioglu.BG-1 as collapsed (when it was actually in a safe state). Fig. 13 reveals the contribution of input features to the prediction result of specimen Lynn. 2CLH18. The red arrows in the figure represent features that positively influence the prediction result towards safe, while the blue arrows represent features that negatively influence the prediction result towards collapse. The base value in the figure is the probability of predicting a safe result without input features. In this study, the number of samples classified as safe in the training dataset was 5878, resulting in a base value of 0.59=5878/10000. When the probability of the prediction being safe is greater than 50%, the predicted result is considered safe. In Fig. 12, the probability that the state of the specimen is safe is 0.71, indicating that the specimen is highly likely to be safe during subsequent earthquakes. The small axial compression ratio and ground motion intensity are the most important features pushing the predicted result towards safe, while the significantly low volume stirrup ratio (0.18%) is the most important feature pushing the predicted result towards collapse.

Fig. 13 reveals the contribution of input features to the prediction result of specimen Saatcioglu. BG-1. The output value in Fig. 14 is 0.495 (less than 0.5), resulting in a predicted collapse. In this figure, more features contribute significantly to the prediction result than in Fig. 13, leading to more complex decisions. As seen from Fig. 14, a smaller volume stirrup ratio and increased axial compression ratio push the predicted result towards collapse, while larger reinforcement strength, smaller ground motion intensity, and smaller damage push the predicted result towards safe. Although the final prediction is collapse, the output value in Fig. 14 is very close to 0.5, indicating that the probability that the sample is actually in a safe state is also high, resulting in the failure of the ML model prediction result. Further evaluation may be required when the predicted probability of the samples approaches 50%. For samples with high collapse or safe probability (collapse or safe probability is more than 80%), the accuracy of the ML prediction model can reach more than 95%. It should be noted that the importance of the prediction for a single sample (Fig. 13-14) may not be the same as the average SHAP value (Fig. 11), as the average SHAP value is a global indicator.

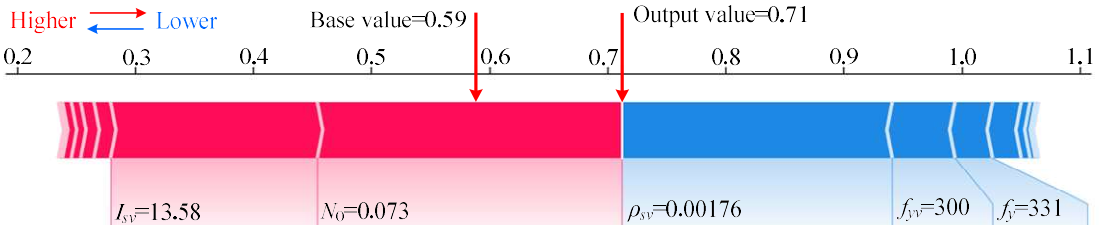

Figure 13. Explanation of the prediction result for specimen Lynn.2CLH18.

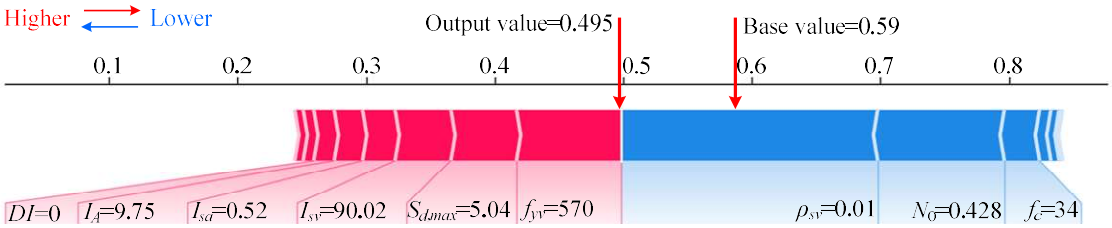

Figure 14. Explanation of the prediction result for specimen Saatcioglu.BG-1.

The summary plots depicted in Fig. 15 can provide insight into the range and distribution of the impact of input features on the prediction results. Each data point in Fig. 15 represents a SHAP value for a given input feature and sample. The vertical axis denotes the relative importance of the input features in descending order, with the color of each point indicating the magnitude of the corresponding input feature, ranging from low (blue) to high (red). Although Fig. 15 bears some resemblance to Fig. 11, there exist some notable differences. Specifically, Fig. 15 illustrates the distribution of SHAP values of each sample and whether the corresponding samples exert a positive or negative influence on the prediction results. For instance, as seen in Fig. 15, an increase in N_0 leads to a corresponding increase in the SHAP value, thereby indicating a higher likelihood of collapse in subsequent earthquakes. Furthermore, the distribution of SHAP values for each feature in Fig. 15 exhibits a distinct color boundary along the vertical axis, implying that each feature exerts a discernible influence on the prediction results. Notably, some samples show that input features with low global importance may still have a significant impact on the prediction results, a finding that is corroborated across Figures 13-15. For example, as evidenced by Fig. 15, the contribution of peak displacement spectrum ($S_{d,max}$) is greater than that of velocity spectrum intensity (I_{sv}). The RF algorithm's ability to capture the varying effects of a given feature across different samples is one of its unique advantages over traditional linear fitting methods.

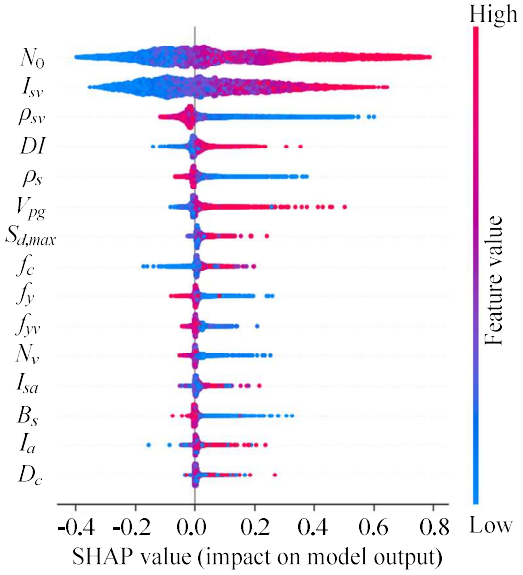

Figure 15. Summary plots for prediction results

Fig. 16 illustrates the SHAP feature dependency, displaying the SHAP value's variation with input features.

Although the SHAP values depicted in Fig. 16 and Fig. 15 are identical, Fig. 16 allows for a better understanding of the distribution and fluctuation of SHAP values across input features. This study analyzes the variation in SHAP value distribution with features and the interaction between different features by selecting some features as examples. Fig. 16(a) shows the impact of axial compression ratio N_0 on the SHAP value when the damage index *DI* varies within its distribution range. The red value represents a high value of the damage index *DI*, while the blue value represents a low value. It can be observed that N_0 has an approximate linear correlation with the SHAP value, and the higher the N_0, the higher the SHAP value. Fig. 16(b) presents the influence of velocity spectral intensity I_{sv} on the SHAP value when the damage index *DI* changes within its distribution range. It is apparent that with the increase of I_{sv}, the SHAP value gradually increases, indicating an increase in collapse risk. However, when I_{sv} is greater than 150cm, the SHAP value's increase is not significant. Fig. 16(c) demonstrates the impact of volumetric stirrup ratio ρ_{sv} on the SHAP value when concrete compressive strength f_c varies within its distribution range. It can be observed that with the increase of ρ_{sv}, the SHAP value gradually decreases, implying a gradual decrease in collapse risk. However, when ρ_{sv} is greater than 0.03, the decline in SHAP value is not significant. Fig. 16(d) shows the influence of damage index *DI* on the SHAP value when axial compression ratio N_0 varies within its distribution range. It can be seen that with the increase of *DI*, the SHAP value has a significant increasing trend. Additionally, the figure also shows a certain interaction between *DI* and N_0. When the damage index *DI* was small (*DI*<0.4), the red spots were mainly concentrated in the upper part of the distribution area, indicating that SHAP value tends to increase with the increase of N_0. When the damage index *DI* was larger (*DI*>0.4), the red dots were not concentrated in the upper part of the distribution area, indicating that RC columns with high damage index *DI*, even those with low axial compression ratio, are susceptible to collapse in subsequent earthquakes.

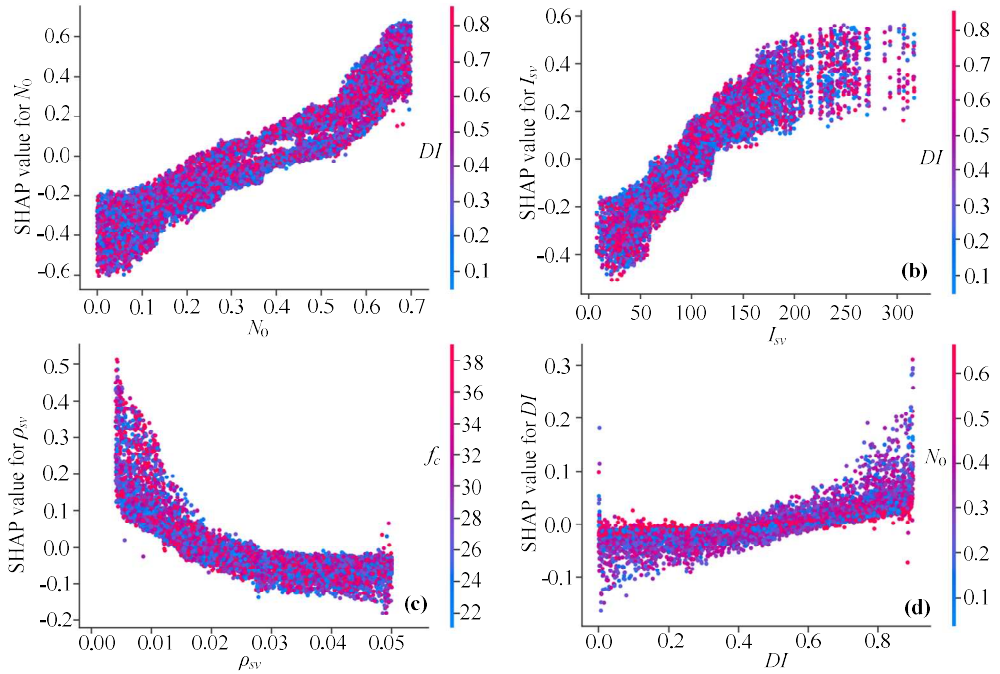

Fig. 16. SHAP dependency plots for collapse probability of the database

5 Interactive graphical user interface

To enable swift evaluation of damaged RC columns after an earthquake, an interactive and user-friendly graphical

user interface (GUI) tool was developed based on the developed ML model, as shown in Fig. 17. The developed tool requires only the input of the design parameters of the RC column and the damage index *DI*. The tool allows for the direct loading of ground motion records by selecting the “Upload ground motion file” button. Once loaded, the necessary intensity parameters of the ground motion records are automatically calculated and displayed on the output page of the tool. Afterward, by clicking the "Predict" button, the probability of the collapse state and the probability of the damaged RC column under subsequent earthquakes can be predicted and displayed. The developed tool can be available in the attachments.

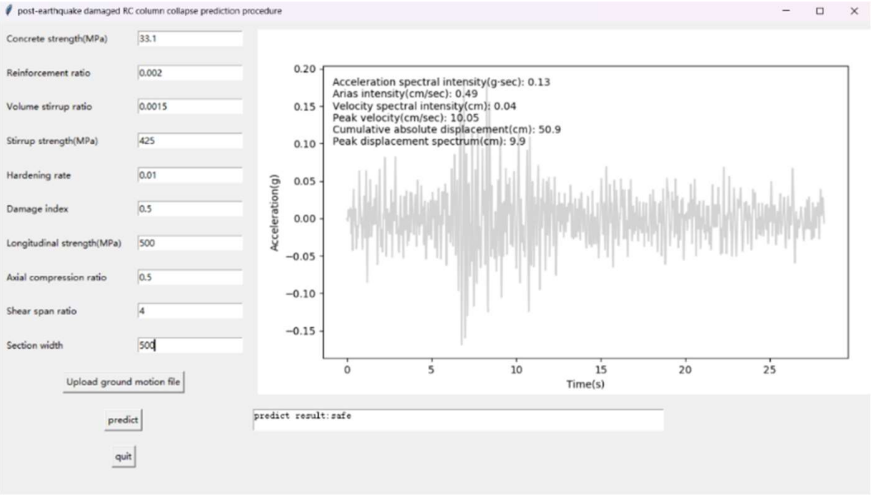

Fig. 17. Graphical user interface for rapid seismic collapse state assessment of post-earthquake damaged RC columns

5 Conclusions

In this study, machine learning method is used to predict the collapse state of post-earthquake damaged RC columns under subsequent earthquakes. The major conclusions are as follows:

(1) A dataset was generated based on a non-linear time history analysis of 10000 post-earthquake damaged RC columns subjected to 1000 ground motions in OpenSees software. The testing data set was generated using the test data of 47 RC columns in PEER database.

(2) Random forest algorithm is used to train an ML prediction model to predict the collapse state of post-earthquake damaged RC columns under subsequent earthquakes. The AUC value and F1 measure were used to test the accuracy of the prediction model. The AUC value and F1 measure of the prediction result were 0.87 and 0.76, respectively, indicating that the prediction model had high accuracy.

(3) The SHAP algorithm is used to explain the prediction model. The results show that the five features that have the greatest influence on the collapse state of damaged RC columns are axial compression ratio N_0, velocity spectral intensity I_{sv}, volumetric stirrup ratio ρ_{sv}, damage index *DI*, and section reinforcement ratio ρ_s. Among them, N_0, I_{sv}, and *DI* have positive effects on RC column collapse, while ρ_{sv} and ρ_s have negative effects. The contribution of the same feature in different samples may be different. SHAP algorithm can decompose the model prediction results into the sum of contributions of different features at the individual scale.

(4) A user-friendly graphical user interface (GUI) tool for identifying the collapse states of post-earthquake

damaged RC columns under subsequent earthquakes based on the ML model was developed to facilitate rapid and accurate post-earthquake assessment.

Acknowledgments

The authors would like to acknowledge the constructive comments provided by 2 responsible reviewers, which helped to improve this paper. This study is sponsored by the National Natural Science Foundation of China (Grant Number:52278531) and the Independent Research and Development project of the State Key Laboratory of Green Building in Western China (Project Number: LSZZ202226).

References

[1] Xie X, Qu Z, Fu H, et al. Effect of prior in-plane damage on the out-of plane behavior of masonry infill walls. Engineering Structures, 2021, 226:111,380. https://doi.org/10.1016/j.engstruct.2020.111380

[2] Cimellaro G, Reinhorn A, and Bruneau M. Framework for analytical quantification of disaster resilience. Engineering Structures, 2010, 32(11): 3639–3649. https://doi.org/10.1016/j.engstruct.2010.08.008

[3] Cimellaro G, Reinhorn A, and Bruneau M. Performance-based metamodel for healthcare facilities. Earthquake Engineering and Structural Dynamics, 2011, 40(11): 1197–1217. https://doi.org/10.1061/(ASCE).EM.1943-7889.0000201

[4] ATC-20. Procedures for post-earthquake building safety evaluation procedures. Redwood City, 1995, CA: Applied Technology Council (ATC).

[5] FEMA 306. Evaluation of earthquake damaged concrete and masonry wall buildings: basic procedures manual. Washington, 1998, DC: Federal Emergency Management Agency.

[6] GB/T 24335−2009. Classification of earthquake damageto buildings and special structures. 2009, Beijing: Standards Press of China.

[7] Alipour M, Harris D, Miller G. Robust pixel-level crack detection using deep fully convolutional neural networks. Journal of Computing in Civil Engineering, 2019, 33(6): 04019040. https://doi.org/10.1061/(ASCE)CP.1943-5487.0000854

[8] Fu F. Fire induced progressive collapse potential assessment of steel framed buildings using machine learning. Journal of Constructional Steel Research, 2020, 166:105918. https://doi.org/10.1016/j.jcsr.2019.105918

[9] Mangalathu S, Jeon J. Stripe-based fragility analysis of multispan concrete bridge classes using machine learning techniques. Earthquake Engineering and Structural Dynamics, 2019, 48(11):1238–55. https://doi.org/10.1002/eqe.3183

[10] Mangalathu S, Sun H, Nweke C, et al. Classifying earthquake damage to buildings using machine learning. Earthquake Spectra, 2020, 36(1):183–208. https://doi.org/10.1177/8755293019878137

[11] Mangalathu S, Hwang S, Jeon J. Failure mode and effects analysis of RC members based on machine learning-based SHapley Additive exPlanations (SHAP) approach. Engineering Structures, 2020, 219:110927. https://doi.org/10.1016/j.engstruct.2020.110927

[12] Harirchian E, Kumari V, Jadhav K, et al. A synthesized study based on machine learning approaches for rapid classifying earthquake damage grades to RC buildings. Applied Sciences, 2021, 11:7540. https://doi.org/10.3390/app11167540

[13] Zhang Y, Burton H, Sun H, et al. A machine learning framework for assessing post-earthquake structural safety. Structural safety, 2018, 72: 1-16. https://doi.org/10.1016/j.strusafe.2017.12.001

[14] Miao Z, Ji X, Wu M, et al. Deep learning-based evaluation for mechanical property degradation of seismically damaged RC columns. Earthquake Engineering and Structural Dynamics, 2022. https://doi.org/10.1002/eqe.3749
[15] Xiong C, Li Q, Lu X. Automated regional seismic damage assessment of buildings using an unmanned aerial vehicle and a convolutional neural network. Automation in Construction, 2020, 109:102,994. https://doi.org/10.1016/j.autcon.2019.102994
[16] Jang Y. Cascaded deep learning network for post-earthquake bridge serviceability assessment. South Dakota State University, 2021.
[17] Luo H, Paal S. A locally weighted machine learning model for generalized prediction of drift capacity in seismic vulnerability assessments, Computer-Aided Civil and Infrastructure Engineering, 2019, 34: 935–950. https://doi.org/10.1111/mice.12456
[18] Luo H, Paal S. Artificial intelligence-enhanced seismic response prediction of reinforced concrete frames, Advanced Engineering Informatics, 2022, 52, 101568. https://doi.org/10.1016/j.aei.2022.101568
[19] Luo H, Paal S. Data-driven seismic response prediction of structural components, Earthquake Spectra, 2022, 38: 1382–1416. https://doi.org/10.1177/87552930211053345
[20] Paal S, Jeon J, Brilakis I, et al. Automated damage index estimation of reinforced concrete columns for post-earthquake evaluations, Journal of Structural Engineering, 2015, 141, 04014228. https://doi.org/10.1061/(ASCE)ST.1943-541X.0001200
[21] Salami MR, Afsar Dizaj E, Kashani MM. Fragility analysis of rectangular and circular reinforced concrete columns under bidirectional multiple excitations, Engineering Structures, 2021, 233, 111887, https://doi.org/10.1016/j.engstruct.2021.111887
[22] Abdelnaby A, Elnashai A. Performance of Degrading Reinforced Concrete Frame Systems under Tohoku and Christchurch Earthquake Sequences. Journal of Earthquake Engineering, 2014, Vol. 18(7) pp. 1009-1036 DOI:10.1080/13632469.2014.923796.
[23] Lu X, Cheng Q, Xu Z, et al. Regional seismic-damage prediction of buildings under mainshock-aftershock sequence. Frontiers of Engineering Management, 2021, 8:122–134. https://doi.org/10.1007/s42524-019-0072-x
[24] Maffei J, Telleen K, Nakayama Y. Probability-based seismic assessment of buildings, considering post-earthquake safety. Earthquake Spectra, 2008, 24(3): 667-699. https://doi.org/10.1193/1.2950066
[25] Yeo G, Cornell C. Building tagging criteria based on aftershock PSHA. 13th World Conference on Earthquake Engineering No. 3283, 2004.
[26] Raghunandan M, Liel A, Luco N. Aftershock collapse vulnerability assessment of reinforced concrete frame structures. Earthquake Engineering and Structural Dynamics, 2015, 44(3):419–439. https://doi.org/10.1002/eqe.2478
[27] Burton H, Deierlein G. Integrating visual damage simulation, virtual inspection, and collapse capacity to evaluate post-earthquake structural safety of buildings. Earthquake Engineering and Structural Dynamics, 2018, 47(2):294–310. https://doi.org/10.1002/eqe.2951
[28] Shokrabadi M, Burton H. Risk-based assessment of aftershock and mainshock-aftershock seismic performance of reinforced concrete frames. Structural Safety, 2018, 73:64–74. https://doi.org/10.1016/j.strusafe.2018.03.003
[29] Abdelnaby A. Fragility curves for RC frames subjected to tohoku mainshock-aftershocks sequences. Journal of Earthquake Engineering, 2018, 22(5):902–920. https://doi.org/10.1080/13632469.2016.1264328
[30] Iervolino I, Chioccarelli E, Suzuki A. Seismic damage accumulation in multiple mainshock–aftershock sequences. Earthquake Engineering and Structural Dynamics, 2020, 49(10):1007–1027. https://doi.org/10.1002/eqe.3275
[31] Liao W, Fei Y, Cheng Q, et al. Influence of accelerometer type on uncertainties in recorded ground motions and

seismic damage assessment. Bulletin of Earthquake Engineering, 2022, 20(9):4419-4439. https://doi.org/10.1007/s10518-022-01461-5
[32] Li L, Luo G, Wang Z, et al. Prediction of residual behaviour for post-earthquake damaged reinforced concrete column based on damage distribution model. Engineering Structures, 2021, 234:111,927. https://doi.org/10.1016/j.engstruct.2021.111927
[33] Kent D, Park R. Flexural members with confined concrete, Journal of the Structural Division, 1971, 97, 1969-1990. https://doi.org/10.1061/JSDEAG.0002957.
[34] Mander J, Priestley M, Park R. Theoretical stress-strain model for confined concrete. Journal of Structural Engineering, 1988, 114(8), 1804-1826. https://doi.org/10.1061/(ASCE)0733-9445(1988)114:8(1804).
[35] Feng D, Ren X. Enriched Force-Based Frame Element with Evolutionary Plastic Hinge. Journal of Structural Engineering, 2017, 143(10): 06017005.1-06017005.7.
[36] Feng D, Ren X, Li J. Implicit Gradient Delocalization Method for Force-Based Frame Element. Journal of Structural Engineering, 2016, 142(2): 04015122.
[37] GB 50011-2010. Code for seismic design of buildings. 2010, Beijing: Standards Press of China.
[38] Marhuenda Y, Morales D, Pardo M. A comparison of uniformity tests. Statistics, 2005, 39(4): 315-327.
[39] Chiofolo C, Chbat N, Ghosh E, et al. Automated continuous acute kidney injury prediction and surveillance: a random forest model. Mayo Clinic Proceedings, 2019, 94(5): 783-792.
[40] Ang B, Priestley M, Park N. Ductility of reinforced bridge piers under seismic loading, Canterbury, New Zealand, 1981. http://dx.doi.org/10.26021/2262
[41] Soesianawati, M.T. Limited ductility design of reinforced concrete columns, Canterbury, New Zealand, 1986. http://dx.doi.org/10.26021/2554
[42] Watson S. Design of Reinforced Concrete Frames of Limited Ductility, Canterbury, New Zealand, 1989. http://dx.doi.org/10.26021/1426
[43] Tanaka H. Effect of lateral confining reinforcement on the ductile behaviour of reinforced concrete columns, Canterbury, New Zealand, 1990. http://dx.doi.org/10.26021/3137
[44] Ohno T, Nishioka Y. An experimental study on energy absorption capacity of columns in reinforced concrete structures. Doboku Gakkai Ronbunshu, 1984, 23-33. https://doi.org/10.2208/JSCEJ.1984.350_23
[45] Atalay M, Penzien J. The seismic behavior of critical regions of reinforced concrete components as influenced by moment, shear and axial force. Berkeley, CA, USA: Earthquake Engineering Research Center, University of California, 1975.
[46] Azizinamini A, Corley W, Johal L. Effects of transverse reinforcement on seismic performance of columns. Aci Structural Journal, 1992, 89, 442-450. https://doi.org/10.14359/3030
[47] Wehbe N. EERI annual student paper award confinement of rectangular bridge columns in moderate seismic areas. Earthquake Spectra, 1988, 14(2), 397-406. https://doi.org/10.1193/1.1586007
[48] Lynn A, Moehle J, Mahin S, et al. Seismic evaluation of existing reinforced concrete building columns. Earthquake Spectra, 1996, 12(4), 715-739. http://dx.doi.org/10.1193/1.1585907
[49] Saatcioglu M, Grira M. Confinement of reinforced concrete columns with welded reinforced grids. Aci Structural Journal, 1999, 96, 29-39. https://doi.org/10.14359/593
[50] Mo Y, Wang S. Seismic behavior of RC columns with various tie configurations. Journal of Structural Engineering, 2000, 126, 1122-1130. https://doi.org/10.1061/(ASCE)0733-9445(2000)126:10(1122)
[51] Takemura H, Kawashima K. Effect of loading hysteresis on ductility capacity of reinforced concrete bridge piers.

Journal of Structural Engineering, 1997, 43, 849-858.
[52] Park Y, Ang, Alfredo H.-S. Mechanistic seismic damage model for reinforced concrete. Journal of Structural Engineering, 1985, 111(4): 722-739.
[53] Wu Z, Han X, Ma J, et al. Sensitivity analysis of ground motion intensity measures and evaluation of potential damage based on machine learning. Journal of Building Structures, 2022. https://doi.org/10.14006/j.jzjgxb.2022.0258
[54] ASCE. Seismic ealuation and rtrofit of eisting bildings, ASCE 41-17 American Society of Civil Engineers, Reston, Virgnia, United States, 2017.

Appendix

Appendix A. Details of test specimen used in this research (Table A.1)

Table A.1 Details of test specimen used in this research

No.	f_c (Mpa)	f_y (Mpa)	f_{yv} (Mpa)	ρ_s (%)	ρ_{sv} (%)	B_s	N_0	N_v	h (mm)	θ_u (%)
Ang.No.3 [40]	23.6	427	320	1.94	2.8	0.004	0.38	3.22	400	3.12
Ang.No.4 [40]	25	427	280	1.94	2.2	0.004	0.21	3.22	400	3.62
Soes.No.1 [41]	46.5	446	364	1.95	0.9	0.007	0.1	4.7	400	6.25
Soes.No.2 [41]	44	446	360	1.42	1.2	0.004	0.3	4	400	5.3
Soes.No.3 [41]	44	446	364	1.51	0.8	0.012	0.3	4	400	2.8
Soes.No.4 [41]	40	446	255	1.51	0.6	0.005	0.3	4	400	2.8
Watson.No.5 [42]	41	474	372	1.51	0.7	0.005	0.5	4	400	2.5
Watson.No.6 [42]	40	474	388	1.51	0.3	0.005	0.5	4	400	1.5
Watson.No.7 [42]	42	474	308	1.51	1.3	0.005	0.7	4	400	1.12
Watson.No.8 [42]	39	474	372	1.51	0.7	0.005	0.7	4	400	1.12
Watson.No.9 [42]	40	474	308	2.22	2.3	0.006	0.7	3.83	400	2.68
Tanaka.No.1 [43]	25.6	474	333	1.93	2.5	0.004	0.2	3	400	3.5
Tanaka.No.5 [43]	32	511	325	2.93	1.7	0.007	0.1	4.7	550	6
Tanaka.No.7 [43]	32.1	511	325	2.93	2.1	0.007	0.3	4.7	550	5
Ohno.L3 [44]	24.8	362	325	1.51	0.3	0.012	0.032	4	400	4.6
Atalay.No.1S1 [45]	29.1	367	363	1.58	1.8	0.004	0.099	3.11	305	6
Atalay.No.2S1 [45]	30.7	367	363	1.58	1.5	0.004	0.093	3.11	305	4.8
Atalay.No.4S1 [45]	27.6	429	363	2.22	0.9	0.006	0.104	3.83	305	5.3
Atalay.No.5S1 [45]	29.4	429	392	2.22	0.9	0.006	0.195	3.83	305	6
Atalay.No.6S1 [45]	31.8	429	392	2.22	1.5	0.004	0.181	3	305	4.8
Atalay.No.9 [45]	33.3	363	392	1.51	0.9	0.01	0.259	4	305	3.03
Atalay.No.10 [45]	32.4	363	392	1.51	1.5	0.01	0.266	4	305	3.03
Azizinamini.NC-2 [46]	39.3	439	454	1.63	0.9	0.004	0.206	5.5	457	4.7
Azizinamini.NC-4 [46]	39.8	439	616	1.63	2.2	0.004	0.31	5.5	457	2.9
Wehbe.A1 [47]	27.2	448	428	1.94	1.9	0.01	0.098	3	610	5.2
Wehbe.A2 [47]	27.2	448	428	1.3	0.4	0.01	0.239	3	610	5.2
Wehbe.B1 [47]	28.1	448	428	1.51	0.4	0.012	0.092	4	610	6.85
Wehbe.B2 [47]	28.1	448	428	1.25	0.5	0.008	0.232	3	610	4.83

Lynn.2CLH18 [48]	33.1	331	299	1.57	0.5	0.005	0.073	4	457.2	2
Lynn.2CMH18 [48]	25.5	331	399	1.25	0.2	0.005	0.284	3	457.2	1
Saatcioglu.BG-1 [49]	34	455.6	570	1.63	0.2	0.004	0.428	5.5	350	3.04
Saatcioglu.BG-2 [49]	34	455.6	570	1.63	1	0.004	0.428	5.5	350	5
Saatcioglu.BG-3 [49]	34	455.6	570	1.63	2	0.004	0.2	5.5	350	7
Saatcioglu.BG-4 [49]	34	455.6	570	1.63	2	0.004	0.462	5.5	350	4.86
Saatcioglu.BG-5 [49]	34	455.6	570	1.63	1.3	0.004	0.462	5.5	350	6
Saatcioglu.BG-8 [49]	34	455.6	580	2.14	2.7	0.003	0.231	3.5	350	7
Mo.C1-1 [50]	24.9	497	459	2.14	1.3	0.003	0.113	3.5	400	6.3
Mo.C1-2 [50]	26.7	497	459	2.14	1.5	0.003	0.158	3.5	400	6.7
Mo.C1-3 [50]	26.1	497	459	1.95	1.5	0.007	0.216	4.7	400	6.65
Takemura.Test1 [51]	35.9	363	368	1.95	1.5	0.007	0.027	4.7	400	3.5
Takemura.Test2 [51]	35.7	363	368	2.93	0.5	0.007	0.027	4.7	400	5.6

Table A.2 Damage strain of the extreme fibers of confined concrete on the bottom sections of the test columns (e=0, γ=c/h)

Specimen	$\varepsilon_d(e, \gamma)$ /%				ε_{ccu}
	Slight	Moderate	Severe	Extreme	/%
Ang.No.3 [40]	1.24	3.51	14.88	84.1	7.67
Ang.No.4 [40]	0.95	2.67	11.33	64.03	5.6
Soes.No.1 [41]	0.54	1.52	6.43	36.31	2.64
Soes.No.2 [41]	0.66	1.88	7.95	44.91	3.53
Soes.No.3 [41]	0.54	1.52	6.43	36.31	2.62
Soes.No.4 [41]	0.42	1.2	5.07	28.67	1.7
Watson.No.5 [42]	0.69	1.96	8.29	46.83	3.68
Watson.No.6 [42]	0.48	1.36	5.75	32.49	2.27
Watson.No.7 [42]	0.85	2.39	10.15	57.34	5
Watson.No.8 [42]	0.73	2.08	8.79	49.69	3.3
Watson.No.9 [42]	1.4	3.95	16.74	94.61	7.42
Tanaka.No.1 [43]	1.24	3.51	14.88	84.1	7.58
Tanaka.No.5 [43]	0.85	2.39	10.15	57.34	4.84
Tanaka.No.7 [43]	0.97	2.75	11.67	65.94	3.3
Ohno.L3 [44]	0.57	1.6	6.77	38.23	2.9
Atalay.No.1S1 [45]	0.78	2.19	9.3	52.56	3.41
Atalay.No.2S1 [45]	0.51	1.44	6.09	34.4	2.38
Atalay.No.4S1 [45]	0.54	1.52	6.43	36.31	2.57
Atalay.No.5S1 [45]	0.81	2.27	9.64	54.47	3.57
Atalay.No.6S1 [45]	0.52	1.48	6.26	35.36	2.45
Atalay.No.9 [45]	0.75	2.12	8.96	50.65	3.28
Atalay.No.10 [45]	0.51	1.44	6.09	34.4	2.42
Azizinamini.NC-2 [46]	1.02	2.87	12.18	68.81	4.02
Azizinamini.NC-4 [46]	0.86	2.43	10.32	58.29	2.05
Wehbe.A1 [47]	0.48	1.36	5.75	32.49	1.84

Wehbe.A2 [47]	0.48	1.36	5.75	32.49	1.84
Wehbe.B1 [47]	0.54	1.52	6.43	36.31	2.15
Wehbe.B2 [47]	0.54	1.52	6.43	36.31	2.15
Lynn.2CLH18 [48]	0.3	0.84	3.55	20.07	0.94
Lynn.2CMH18 [48]	0.3	0.84	3.55	20.07	1.1
Saatcioglu.BG-1 [49]	0.65	1.84	7.78	43.96	3.07
Saatcioglu.BG-2 [49]	1.19	3.35	14.21	80.27	4.5
Saatcioglu.BG-3 [49]	1.19	3.35	14.21	80.27	4.5
Saatcioglu.BG-4 [49]	0.79	2.23	9.47	53.52	3.7
Saatcioglu.BG-5 [49]	1.47	4.15	17.59	99.39	5.28
Saatcioglu.BG-8 [49]	0.95	2.67	11.33	64.03	3.41
Mo.C1-1 [50]	1.19	3.35	14.21	80.27	3.95
Mo.C1-2 [50]	1.13	3.19	13.53	76.45	3.78
Mo.C1-3 [50]	1.13	3.19	13.53	76.45	3.78
Takemura.Test1 [51]	0.45	1.28	5.41	30.58	1.28
Takemura.Test2 [51]	0.45	1.28	5.41	30.58	1.28

1